

UC San Diego

UC San Diego Previously Published Works

Title

Long-distance decay-less spin transport in indirect excitons in a van der Waals heterostructure.

Permalink

<https://escholarship.org/uc/item/443152sv>

Journal

Nature Communications, 15(1)

Authors

Zhou, Zhiwen

Szwed, E

Choksy, D

et al.

Publication Date

2024-11-01

DOI

10.1038/s41467-024-53445-5

Peer reviewed


Long-distance decay-less spin transport in indirect excitons in a van der Waals heterostructure

Received: 15 May 2024

Zhiwen Zhou , E. A. Szwed, D. J. Choksy, L. H. Fowler-Gerace & L. V. Butov  

Accepted: 8 October 2024

Published online: 01 November 2024

 Check for updates

In addition to its fundamental interest, the long-distance spin transport is essential for spintronic devices. However, the spin relaxation caused by scattering of the particles carrying the spin limits spin transport. We explored spatially indirect excitons (IXs) in van der Waals heterostructures composed of atomically thin layers of transition-metal dichalcogenides as spin carriers. We observed the long-distance spin transport: the spin polarized excitons travel over the entire sample, ~ 10 micron away from the excitation spot, with no spin density decay. This transport is characterized by the $1/e$ decay distances reaching ~ 100 micron. The $1/e$ decay distances are extracted from fits over the ~ 10 micron sample size. The emergence of long-distance spin transport is observed at the densities and temperatures where the IX transport decay distances and, in turn, scattering times are strongly enhanced. The suppression of IX scattering suppresses the spin relaxation and enables the long-distance spin transport.

The physics of spin transport includes a number of fundamental phenomena, such as the current-induced spin orientation (the spin Hall effect)^{1–4}, the spin drift, diffusion and drag^{5–7}, the quantum spin Hall effect^{8–10}, and the persistent spin helix¹¹. In addition to its fundamental interest, long-distance spin transport with suppressed spin losses is essential for developing spintronic devices, which may offer advantages in dissipation, size, and speed over charge-based devices¹².

Spatially indirect excitons (IXs), also known as interlayer excitons, in heterostructures (HS) can enable the realization of the long-distance spin transfer. IXs are composed of electrons and holes confined in separated layers¹³. Due to the separation of electron and hole layers, the IX lifetimes can exceed the lifetimes of spatially direct excitons (DXs) by orders of magnitude. Due to their long lifetimes, IXs can cool down below the temperature of quantum degeneracy and form a condensate¹⁴ and can travel over long distances¹⁵. Traveling particles can transfer the spin state. However, the particle scattering causes fluctuating effective magnetic fields originating from the spin-orbit interaction in noncentrosymmetric materials and, as a result, causes the spin relaxation that limits the spin transfer¹⁶. Therefore, the range of spin transport can be extended by suppressing the scattering of the particles carrying the spin states. This can be achieved with IXs: The suppression of scattering in IX condensate can suppress the spin

relaxation and allow long-distance spin transport. In addition, in contrast to DXs, the electron-hole separation in IXs suppresses the overlap of the electron and hole wave functions and, as a result, suppresses the spin relaxation due to electron-hole exchange¹⁷.

IXs can be created in various HS, in particular, in GaAs HS^{18–22}, in GaN HS²³, and in ZnO HS²⁴. Since the temperature of quantum degeneracy, which can be achieved for excitons, scales proportionally to the exciton binding energy E_X ²⁵, IXs with high E_X can form a platform for the realization of high-temperature long-distance spin transport.

IXs in GaAs HS have low $E_X \lesssim 10$ meV^{26,27}, and the highest $E_X \sim 30$ meV for IXs in III–V and II–VI semiconductor HS is achieved in ZnO HS²⁴. Van der Waals HS composed of atomically thin layers of transition-metal dichalcogenides (TMD) enable the realization of excitons with remarkably high binding energies^{28–31} and E_X for IXs in TMD HS reach hundreds of meV^{25,32,33}.

TMD HS also give an opportunity to explore spin transport in periodic potentials due to moiré superlattices. The period of the latter $b \approx a/\sqrt{\delta\theta^2 + \delta^2}$ is typically in the 10 nm range (a is the lattice constant, δ the lattice mismatch, $\delta\theta$ the deviation of the twist angle between the layers from $i\pi/3$, i is an integer)^{34–49}. The moiré potentials can be affected by atomic reconstruction^{50–52} and by the disorder.

In addition, due to the coupling of the spin and valley indices in TMD HS^{53–56}, the spin transport is coupled to the valley transport (therefore, for simplicity, we will use the term ‘spin’ also for ‘spin-valley’).

Detecting the transport of spin-polarized excitons via spatially- and polarization-resolved imaging of exciton luminescence gives the direct measurement of spin transport. Earlier studies using this method led to the observation of spin transport with $1/e$ decay distances $d_{1/e}^s$ up to a few μm in IXs in TMD HS^{57–60}. Spin transport with $d_{1/e}^s$ of a few μm was also observed in DXs⁶¹, and the excitation-induced polarization was found to lead to the emergence of ferromagnetic order⁶² and to electron or hole spin transport with a spin diffusion length up to ca. 20 μm ^{63,64} in TMD. Spin relaxation due to scattering of the particles carrying the spin-limited spin transport distances¹⁶.

In this work, we observed in a $\text{MoSe}_2/\text{WSe}_2$ HS the IX mediated long-distance spin transport: the spin polarized excitons travel over the entire sample, ~ 10 micron away from the excitation spot, with no spin density decay. This transport is characterized by the $1/e$ decay distances reaching ~ 100 μm . The long-distance spin transport vanishes at high temperatures. With increasing IX density, we observed spin localization, then long-distance spin transport, and then reentrant spin localization.

Results

$\text{MoSe}_2/\text{WSe}_2$ heterostructure

We study $\text{MoSe}_2/\text{WSe}_2$ HS assembled by stacking mechanically exfoliated 2D crystals [Supplementary Fig. S1]. IXs are formed from

electrons and holes confined in adjacent MoSe_2 and WSe_2 monolayers (ML), respectively, encapsulated by hBN layers. No voltage is applied in the HS. IXs form the lowest-energy exciton state in the $\text{MoSe}_2/\text{WSe}_2$ HS (Supplementary Fig. S1). The HS details are presented in SI.

IX generation and detection

Both the long-distance IX transport⁶⁵ and the long-distance spin transport, which is described below, are realized when the optical excitation has the energy E_{ex} close to the energy of DXs in the HS. The resonant excitation allows for lowering the excitation-induced heating of the IX system. In particular, the colder IXs created by the resonant excitation screen the HS disorder more effectively^{66–68}. In this work, the laser excitation with $E_{\text{ex}} = 1.689$ eV is resonant to WSe_2 DX.

Both spin generation and detection in IXs are achieved by optical means via photon polarization. The circularly polarized laser excitation is focused to a ~ 2 μm spot, and the spin propagation is detected by the polarization-resolved PL imaging. Figure 1a shows a high degree of circular polarization in the excitation spot, indicating an effective transfer of the optically generated spin-polarized DXs to the spin-polarized IXs with the spin relaxation time long compared to the exciton recombination and energy relaxation times.

IX-mediated spin transport

The propagation of spin-polarized IXs from the excitation spot transfer the spin polarization. For the particular IX densities and temperatures,

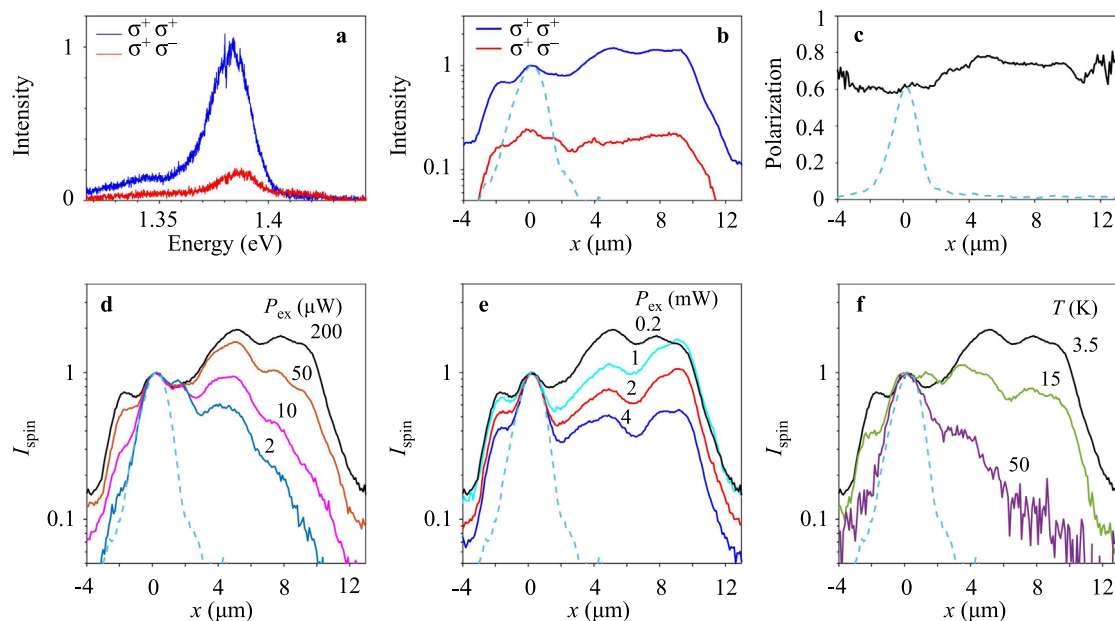


Fig. 1 | The long-distance spin-valley transport in IXs in $\text{MoSe}_2/\text{WSe}_2$ HS. **a** The circular polarization of IX PL. The blue (red) spectrum is co-polarized (cross-polarized) with the circularly polarized laser excitation. **b** Co-polarized I_{σ^+} (blue) and cross-polarized I_{σ^-} (red) IX PL intensity vs. the distance from the laser excitation spot centered at $x = 0$. The HS active area extends from $x \sim -3$ to 10 μm . The polarized IX PL propagates through the entire HS. **c** The degree of circular polarization of IX PL $P = (I_{\sigma^+} - I_{\sigma^-}) / (I_{\sigma^+} + I_{\sigma^-})$ vs. the transport distance. No decay is observed for the polarization transport for IXs over the entire HS. The laser excitation power $P_{\text{ex}} = 0.2$ mW, $T = 1.7$ K (**a–c**). **d–f** Normalized spin density profiles $I_{\text{spin}} = I_{\sigma^+} - I_{\sigma^-}$ for the LE-IXs for different P_{ex} (**d, e**) and temperatures (**f**). In (**d**),

$P_{\text{ex}} = 2, 10, 50, 200$ μW (bottom to top). In (**e**), $P_{\text{ex}} = 0.2, 1, 2, 4$ mW (top to bottom). In (**c**), $T = 3.5, 15, 50$ K (top to bottom). The spin density transport non-monotonically varies with increasing P_{ex} , increases at $P_{\text{ex}} \lesssim 0.2$ mW (**d**) and reduces at $P_{\text{ex}} \geq 0.2$ mW (**e**), and vanishes at high temperatures (**f**). The dashed line in (**b–f**) shows the DX luminescence profile in the MoSe_2 ML, this profile is close to the laser excitation profile for short-range DX transport. The LE-IX spectra are separated from the HE-IX spectra by the spectral integration in the range $E < 1.4$ eV (**b–f**). The HE-IXs appear in the spectra at high $P_{\text{ex}} \geq 0.2$ mW (Fig. 3). $T = 3.5$ K (**d, e**), $P_{\text{ex}} = 0.2$ mW (**f**). The ~ 2 μm laser spot is centered at $x = 0$ (**a–f**).

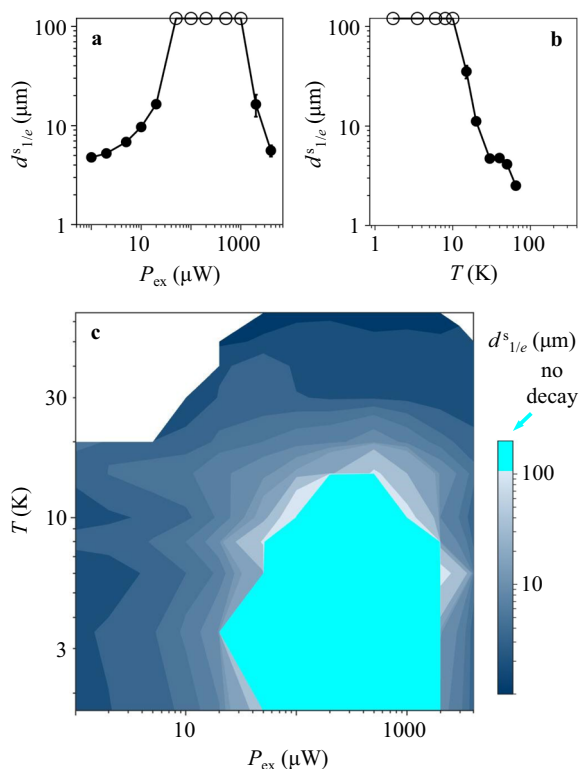


Fig. 2 | Excitation power and temperature dependence of spin transport in LE-IXs. **a–c** The $1/e$ decay distance $d_{1/e}^s$ of spin density transport $I_{\text{spin}} = I_{\sigma^+} - I_{\sigma^-}$ in LE-IXs vs. the laser excitation power P_{ex} (**a**), vs. temperature (**b**), and vs. P_{ex} and temperature (**c**). $d_{1/e}^s$ are obtained from least-squares fitting the LE-IX spin density transport profiles $I_{\text{spin}}(x)$ (Fig. 1d–f) to exponential decays in the region from the excitation spot to the HS edge, $x = 0 - 9 \mu\text{m}$. The data with the fit indicating diverging $d_{1/e}^s$ are presented by circles on the edge (**a**, **b**) or by cyan color (**c**). The error bars represent the uncertainty in least-squares fitting the spin transport decays to exponential decays. The LE-IX spectra are separated from the HE-IX spectra by the Gaussian fits. The HE-IXs appear in the spectra at high $P_{\text{ex}} \geq 0.2 \text{ mW}$ (Fig. 3). $T = 3.5 \text{ K}$ (**a**), $P_{\text{ex}} = 0.2 \text{ mW}$ (**b**).

outlined below, both the intensities of co-polarized and cross-polarized IX PL I_{σ^+} and I_{σ^-} (Fig. 1b) and the degree of circular polarization of IX PL $P = (I_{\sigma^+} - I_{\sigma^-}) / (I_{\sigma^+} + I_{\sigma^-})$ (Fig. 1c) propagate over the entire HS with no losses.

IX transport is characterized by the propagation of total IX intensity in both circular polarizations $n \sim I_{\sigma^+} + I_{\sigma^-}$. In turn, the transport of spin polarization density carried by IXs is characterized by the propagation of $I_{\text{spin}} = Pn = I_{\sigma^+} - I_{\sigma^-}$. The dependence of spin density transport on excitation power P_{ex} and temperature is described below. The spin transport nonmonotonically varies with increasing P_{ex} , increases at $P_{\text{ex}} \lesssim 0.2 \text{ mW}$ (Fig. 1d) and reduces at $P_{\text{ex}} \geq 0.2 \text{ mW}$ (Fig. 1e), and vanishes at high temperatures (Fig. 1f). The spin transport is characterized by the $1/e$ decay distance of the spin polarization density $d_{1/e}^s$. The latter is obtained from least-squares fitting the spin density transport profiles $I_{\text{spin}}(x)$ (Fig. 1d–f) to exponential decays in the region from the excitation spot to the HS edge. The variation of spin transport with excitation power and temperature is presented by the variation of $d_{1/e}^s$ in Fig. 2. The HS dimensions allow establishing that the longest $d_{1/e}^s$ reach $100 \mu\text{m}$ (as outlined in Supplementary Note 6). The data with the fit indicating diverging $d_{1/e}^s$, that is, with no spin density decay within the entire HS, are presented by circles on the edge in Fig. 2a, b, and by cyan color in Fig. 2c.

For low P_{ex} , a single IX PL line is observed in the spectra. However, a higher-energy IX PL line appears in the spectrum at high P_{ex} (Fig. 3).

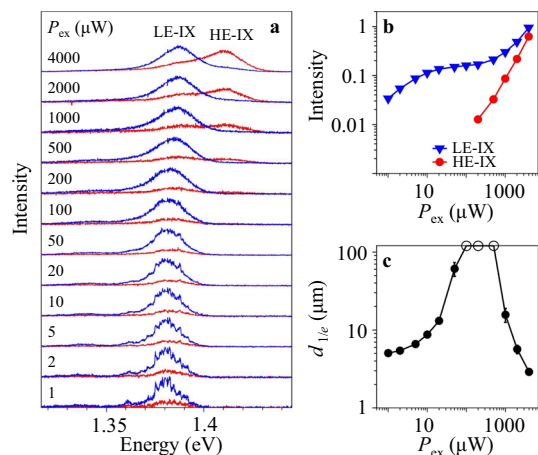


Fig. 3 | Density dependence of IX PL spectra. **a** The excitation power P_{ex} dependence of co-polarized (blue) and cross-polarized (red) IX spectra. The lower-energy IX (LE-IX) PL is co-polarized. The higher-energy IX (HE-IX) PL is cross-polarized. The HE-IXs appear in the spectra at high $P_{\text{ex}} \geq 0.2 \text{ mW}$. The spectral profile separation of LE-IXs and HE-IXs is presented in Supplementary Fig. S3. **b** The intensity of LE-IX PL (blue triangles) and HE-IX PL (red points) vs. P_{ex} . **c** The $1/e$ LE-IX transport decay distance $d_{1/e}^s$ vs. P_{ex} . $d_{1/e}^s$ are obtained from least-squares fitting the spectrally integrated LE-IX PL intensity including both polarizations $I_{\sigma^+} + I_{\sigma^-}$ to exponential decays in the region from the excitation spot to the HS edge, $x = 0 - 9 \mu\text{m}$. The data with the fit indicating diverging $d_{1/e}^s$ are presented by circles on the edge. The error bars represent the uncertainty in least-squares fitting the LE-IX transport decays to exponential decays. The appearance of HE-IX in the spectrum (**a**, **b**) correlates with the onset of IX transport suppression (**c**). $T = 3.5 \text{ K}$.

We will refer to the IXs corresponding to these PL lines as the lower-energy IXs (LE-IXs) and higher-energy IXs (HE-IXs). Figures 1 and 2 present the spin transport carried by LE-IXs.

Discussion

Comparison of spin transport and IX transport

The data are discussed below. The spin transport (Fig. 2) is carried by LE-IXs and can be compared with the LE-IX transport (Fig. 3c and Supplementary Fig. S7). Due to the separation d_z between the electron and hole layers, IXs have electric dipoles ed_z , and the interaction between IXs is repulsive⁶⁹. IXs in moiré superlattices form a system of repulsively interacting bosons in periodic potentials. The enhancement followed by the suppression of the LE-IX transport with density (Fig. 3c) is in qualitative agreement with the Bose-Hubbard theory of bosons in periodic potentials predicting superfluid at $N - 1/2$ and insulating at $N - 0$ and $N - 1$ phases for the number of bosons per site of the periodic potential N^{70} . For the maximum LE-IX transport distances observed at $P_{\text{ex}} \sim 0.2 \text{ mW}$ (Fig. 3c), the LE-IX density n estimated from the energy shift δE as $n = \delta E \epsilon / (4\pi e^2 d_z)$ ⁶⁹ is $n \sim 2 \times 10^{11} \text{ cm}^{-2}$ ($d_z \sim 0.6 \text{ nm}$, the dielectric constant $\epsilon \sim 7.4$ ⁷¹). This density is well below the Mott transition density $n_{\text{Mott}} > 10^{12} \text{ cm}^{-2}$ ^{25,72}. $N - 1/2$ at $n \sim 2 \times 10^{11} \text{ cm}^{-2}$ for the moiré superlattice period $b = 17 \text{ nm}$. This period $b - a/d\theta$ corresponds to the twist angle $d\theta = 1.1^\circ$, which agrees with the angle between MoSe₂ and WSe₂ edges in the HS (Supplementary Fig. S1). This rough estimate indicates that the observation of LE-IX localization, then long-range transport, and then localization with increasing density (Fig. 3c) is in agreement with the Bose-Hubbard theory⁷⁰.

In contrast, the data disagree with the classical diffusive transport. For classical transport, a substantial increase of transport distance with density occurs when the IX interaction energy becomes comparable to the amplitude of in-plane potential so it can be screened by the repulsively interacting IXs⁶⁸. However, the amplitude of in-plane disorder and moiré potential in MoSe₂/WSe₂ HS, tens of meV^{34–49}, is

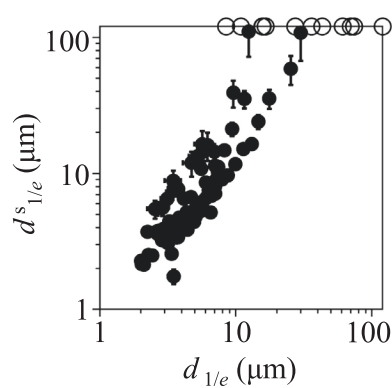


Fig. 4 | Correlation between the spin transport $1/e$ decay distances $d_{1/e}^s$ and the LE-IX transport $1/e$ decay distances $d_{1/e}$. The values for $d_{1/e}^s$ and $d_{1/e}$ are taken from Fig. 2 and Supplementary Fig. S7. The data with the fit indicating diverging $d_{1/e}^s$ and $d_{1/e}$ are presented by circles on the edge. The error bars represent the uncertainty in least-squares fitting the transport decays to exponential decays. The enhancement of $d_{1/e}^s$ with $d_{1/e}$ is observed in a broad range of both excitation density and temperature variations, corresponding to the range of these parameters in Fig. 2 and Supplementary Fig. S7.

significantly higher than the IX interaction energy given by the LE-IX energy shift with density, a few meV (Fig. 3a). Therefore, the IX interaction energy is insufficiently strong to screen the in-plane potential and neither the long-distance decay-less LE-IX transport (Fig. 3c) nor the long-distance decay-less spin transport (Fig. 2) can occur due to classical screening of the in-plane potential⁶⁸. In addition, the transport suppression at high densities (Fig. 3c) is inconsistent with the classical diffusive transport, which enhances with density^{58,60,68}. Furthermore, the long-range transport vanishes at high temperatures (Supplementary Fig. S7), which is inconsistent with the classical diffusive transport, which enhances with temperature^{58,60,68}.

High values of $d_{1/e}$ (Fig. 3c) indicate high values of IX diffusivity. In turn, diffusivities are proportional to scattering times, and high IX diffusivities indicate suppression of IX scattering. For instance, for classical diffusive LE-IX transport, the IX diffusivity and mean free time (scattering time) are given by $\sim (d_{1/e})^2/\tau$ and $\sim (d_{1/e})^2/\tau \cdot m/(k_B T)$, respectively (τ and m are the IX lifetime and mass, m - free electron mass and τ - 10 ns for the HS⁶⁵). These values become anomalously high for $d_{1/e} \sim 100 \mu\text{m}$. However, as outlined above, the long-range IX transport is beyond classical diffusive transport, and, therefore, accurate estimates of IX diffusivities and scattering times should go beyond the formulas for classical diffusion and that is the subject of future works.

The density dependence of spin transport (Fig. 2a) is qualitatively similar to the density dependence of LE-IX transport (Fig. 3c): Both spin transport and LE-IX transport first enhance and then suppress with density. The temperature dependence of spin transport is qualitatively similar to the temperature dependence of LE-IX transport: Both the long-distance spin transport (Fig. 2b) and the long-distance LE-IX transport (Supplementary Fig. S7) vanish at $T \sim 10 \text{ K}$. The parameters for the long-distance decay-less spin transport (Fig. 2) correlate with the parameters for the long-range LE-IX transport (Fig. 3c and Supplementary Fig. S7). Figure 4 shows that the enhancement of $d_{1/e}^s$ with $d_{1/e}$ is observed in a broad range of both excitation density and temperature variations, corresponding to the range of these parameters in Fig. 2 and Supplementary Fig. S7. The correlation of $d_{1/e}^s$ with $d_{1/e}$ and, in turn, enhanced IX scattering time suggests the suppression of scattering as the mechanism of the long-distance decay-less spin transport. This complies with the scattering being the mechanism of spin relaxation that limits the spin transfer¹⁶.

The enhanced $d_{1/e}$ and, in turn, scattering time is observed in the range of temperatures and densities consistent with those predicted

for superfluidity by the Bose-Hubbard theory⁷⁰ as outlined above. Therefore, superfluidity can be the origin of the enhanced scattering time.

The long-distance decay-less spin transport vanishes at $\sim 10 \text{ K}$ (Fig. 2b, c). The mechanism of suppression of spin relaxation due to suppression of scattering of IXs carrying the spin indicates that long-distance spin transport with suppressed losses can be achieved at high temperatures in IX systems with high superfluidity temperatures T_c . The theory predicts that the superfluidity temperature for bosons in periodic potentials $T_c \sim 4\pi N J$ and higher T_c can be achieved in lattices with higher inter-site hopping J ⁷³. Higher J can be achieved in moiré superlattices with smaller periods in HS with larger twist angles $\delta\theta$, or in moiré superlattices with smaller amplitudes that can be realized in HS with the same-TMD electron and hole layers^{74,75}, or by lowering the moiré superlattice amplitude by voltage^{37,76}, or by adding a spacer (hBN) layer between the electron and hole layers⁵⁸. For TMD HS with suppressed moiré potentials, the theory predicts high- T_c superfluidity^{25,32}. This, in turn, can enable the realization of high-temperature long-distance spin transport with suppressed losses.

Lower-energy and higher-energy IXs

The above data outline the long-distance spin transport carried by LE-IXs. Figure 3 shows that HE-IX PL appears in the spectrum at high P_{ex} . In contrast to the LE-IX PL, which is co-polarized, the HE-IX PL is cross-polarized with circularly polarized laser excitation. A similar higher-energy IX PL was observed in earlier studies. Various interpretations for multiple IX PL lines were considered, including the excitonic states split due to the conduction band K-valley spin splitting⁷⁷, trions⁷⁸, excitonic states indirect in momentum space and split due to the valley energy difference^{79,80} or spin-orbit coupling⁸¹, excitonic states in moiré superlattices⁴⁰⁻⁴⁶ and, recently, excitonic states in moiré lattice sites with single and double occupancy^{82,83}. Our data show that the appearance of HE-IX PL in the spectrum (Fig. 3a, b) correlates with the onset of IX reentrant localization (Fig. 3c). As outlined above, in the regime of reentrant localization, the occupation of moiré cells becomes high. This results in the appearance of moiré cells with double occupancy. Therefore, the IX reentrant localization in transport measurements (Fig. 3c) is consistent with the appearance of high-energy IX PL in the spectra (refs. 82,83 and Fig. 3a, b). The intra-cell IX repulsion enhances the IX energy. This is in qualitative agreement with a higher HE-IX energy (Fig. 3a). (Spin transport in HE-IXs is shorter-range than in LE-IXs and is not considered in this work.) (Narrow PL lines at low densities (Fig. 3a) can be related to localized states and are not considered in this work.)

In summary, we observed in a $\text{MoSe}_2/\text{WSe}_2$ HS the IX-mediated long-distance spin transport: the spin-polarized IXs travel over the entire sample, $\sim 100 \mu\text{m}$ away from the excitation spot, with no spin density decay. This transport is characterized by the $1/e$ decay distances reaching $\sim 100 \mu\text{m}$. The emergence of long-distance spin transport is observed at the densities and temperatures where the IX transport decay distances and, in turn, scattering times are strongly enhanced. The suppression of IX scattering suppresses the spin relaxation and enables long-distance spin transport. This mechanism of protection against spin relaxation makes IXs a platform for the realization of long-distance decay-less spin transport.

Methods

Van der Waals HS

The $\text{MoSe}_2/\text{WSe}_2$ HS was assembled using the dry-transfer peel-and-lift technique⁸⁴. The heterostructure details are presented in Supplementary Note 1.

Optical measurements

Excitons were generated by a cw Ti:Sapphire laser with the excitation energy $E_{\text{ex}} = 1.689 \text{ eV}$. PL spectra were measured using a spectrometer with a resolution of 0.2 meV and a liquid-nitrogen-cooled CCD.

The spatial profiles of polarization-resolved IX PL vs. x were obtained from the polarization-resolved PL images detected using the CCD. The signal was integrated from $y = -0.5$ to $y = +0.5 \mu\text{m}$. Representative polarization-resolved IX PL images are presented in Supplementary Note 2.

The experiments were performed in a variable-temperature 4He cryostat. The sample was mounted on an Attocube xyz piezo translation stage allowing adjusting the sample position relative to a focusing lens inside the cryostat. All phenomena presented in this work are reproducible after multiple cooling down to 2 K and warming up to room temperature.

Data availability

Source data files are available via Figshare at <https://doi.org/10.6084/m9.figshare.27003031>. All relevant data are available from the corresponding author upon reasonable request.

References

- D'yakonov, M. I. & Perel', V. I. Current-induced spin orientation of electrons in semiconductors. *Phys. Lett. A* **35**, 459–460 (1971).
- Hirsch, J. E. Spin Hall effect. *Phys. Rev. Lett.* **83**, 1834–1837 (1999).
- Sinova, J. et al. Universal intrinsic spin Hall effect. *Phys. Rev. Lett.* **92**, 126603 (2004).
- Kato, Y. K., Myers, R. C., Gossard, A. C. & Awschalom, D. D. Observation of the spin Hall effect in semiconductors. *Science* **306**, 1910–1913 (2004).
- Kikkawa, J. M. & Awschalom, D. D. Lateral drag of spin coherence in gallium arsenide. *Nature* **397**, 139–141 (1999).
- Weber, C. P. et al. Observation of spin Coulomb drag in a two-dimensional electron gas. *Nature* **437**, 1330–1333 (2005).
- Crooker, S. A. et al. Imaging spin transport in lateral ferromagnet/semiconductor structures. *Science* **309**, 2191–2195 (2005).
- Kane, C. L. & Mele, E. J. Z_2 Topological order and the quantum spin Hall effect. *Phys. Rev. Lett.* **95**, 146802 (2005).
- Bernevig, B. A. & Zhang, S.-C. Quantum spin Hall effect. *Phys. Rev. Lett.* **96**, 106802 (2006).
- König, M. et al. Quantum spin Hall insulator state in HgTe quantum wells. *Science* **318**, 766–770 (2007).
- Koralek, J. D. et al. Emergence of the persistent spin helix in semiconductor quantum wells. *Nature* **458**, 610–613 (2009).
- Awschalom, D. D. & Flatté, M. E. Challenges for semiconductor spintronics. *Nat. Phys.* **3**, 153–159 (2007).
- Lozovik, Y. E. & Yudson, V. I. A new mechanism for superconductivity: pairing between spatially separated electrons and holes. *Zh. Eksp. Teor. Fiz.* **71**, 738–753 (1976).
- High, A. A. et al. Spontaneous coherence in a cold exciton gas. *Nature* **483**, 584–588 (2012).
- Hagn, M., Zrenner, A., Böhm, G. & Weimann, G. Electric-field-induced exciton transport in coupled quantum well structures. *Appl. Phys. Lett.* **67**, 232–234 (1995).
- Dyakonov, M. I. *Spin Physics in Semiconductors* (Springer, New York, 2008).
- Maijale, M. Z., de Andrada e Silva, E. A. & Sham, L. J. Exciton spin dynamics in quantum wells. *Phys. Rev. B* **47**, 15776–15788 (1993).
- Leonard, J. R. et al. Spin transport of excitons. *Nano Lett.* **9**, 4204–4208 (2009).
- High, A. A. et al. Spin currents in a coherent exciton gas. *Phys. Rev. Lett.* **110**, 246403 (2013).
- Violante, A., Hey, R. & Santos, P. V. Coherent transport and manipulation of spins in indirect-exciton nanostructures. *Phys. Rev. B* **91**, 125302 (2015).
- Finkelstein, R. et al. Transition from spin-orbit to hyperfine interaction dominated spin relaxation in a cold fluid of dipolar excitons. *Phys. Rev. B* **96**, 085404 (2017).
- Leonard, J. R. et al. Pancharatnam-Berry phase in condensate of indirect excitons. *Nat. Commun.* **9**, 2158 (2018).
- Chiaruttini, F. et al. Trapping dipolar exciton fluids in GaN/(AlGa)N nanostructures. *Nano Lett.* **19**, 4911–4918 (2019).
- Morhain, C. et al. Internal electric field in wurtzite ZnO/Zn_{0.78}Mg_{0.22}O quantum wells. *Phys. Rev. B* **72**, 241305(R) (2005).
- Fogler, M. M., Butov, L. V. & Novoselov, K. S. High-temperature superfluidity with indirect excitons in van der Waals heterostructures. *Nat. Commun.* **5**, 4555 (2014).
- Zrenner, A. et al. Indirect excitons in coupled quantum well structures. *Surf. Sci.* **263**, 496–501 (1992).
- Sivalertporn, K., Mouchliadis, L., Ivanov, A. L., Philp, R. & Muljarov, E. A. Direct and indirect excitons in semiconductor coupled quantum wells in an applied electric field. *Phys. Rev. B* **85**, 045207 (2012).
- Geim, A. K. & Grigorieva, I. V. Van der Waals heterostructures. *Nature* **499**, 419–425 (2013).
- Ye, Z. et al. Probing excitonic dark states in single-layer tungsten disulphide. *Nature* **513**, 214–218 (2014).
- Chernikov, A. et al. Exciton Binding Energy and Nonhydrogenic Rydberg Series in Monolayer WS₂. *Phys. Rev. Lett.* **113**, 076802 (2014).
- Goryca, M. et al. Revealing exciton masses and dielectric properties of monolayer semiconductors with high magnetic fields. *Nat. Commun.* **10**, 4172 (2019).
- Berman, O. L. & Kezerashvili, R. Y. Superfluidity of dipolar excitons in a transition metal dichalcogenide double layer. *Phys. Rev. B* **96**, 094502 (2017).
- Deilmann, T. & Thygesen, K. S. Interlayer trions in the MoS₂/WS₂ van der Waals heterostructure. *Nano Lett.* **18**, 1460–1465 (2018).
- Wu, F., Lovorn, T. & MacDonald, A. H. Theory of optical absorption by interlayer excitons in transition metal dichalcogenide heterobilayers. *Phys. Rev. B* **97**, 035306 (2018).
- Yu, H., Liu, G.-B. & Yao, W. Brightened spin-triplet interlayer excitons and optical selection rules in van der Waals heterobilayers. *2D Mater.* **5**, 035021 (2018).
- Wu, F., Lovorn, T. & MacDonald, A. H. Topological exciton bands in Moiré heterojunctions. *Phys. Rev. Lett.* **118**, 147401 (2017).
- Yu, H., Liu, G.-B., Tang, J., Xu, X. & Yao, W. Moiré excitons: From programmable quantum emitter arrays to spin-orbit-coupled artificial lattices. *Sci. Adv.* **3**, e1701696 (2017).
- Zhang, C. et al. Interlayer couplings, Moiré patterns, and 2D electronic superlattices in MoS₂/WSe₂ hetero-bilayers. *Sci. Adv.* **3**, e1601459 (2017).
- Rivera, P. et al. Interlayer valley excitons in heterobilayers of transition metal dichalcogenides. *Nat. Nanotechnol.* **13**, 1004–1015 (2018).
- Zhang, N. et al. Moiré intralayer excitons in a MoSe₂/MoS₂ heterostructure. *Nano Lett.* **18**, 7651–7657 (2018).
- Ciarrocchi, A. et al. Polarization switching and electrical control of interlayer excitons in two-dimensional van der Waals heterostructures. *Nat. Photonics* **13**, 131–136 (2019).
- Seidler, K. L. et al. Signatures of moiré-trapped valley excitons in MoSe₂/WSe₂ heterobilayers. *Nature* **567**, 66–70 (2019).
- Tran, K. et al. Evidence for moiré excitons in van der Waals heterostructures. *Nature* **567**, 71–75 (2019).
- Jin, C. et al. Observation of moiré excitons in WSe₂/WS₂ heterostructure superlattices. *Nature* **567**, 76–80 (2019).
- Alexeev, E. M. et al. Resonantly hybridized excitons in moiré superlattices in van der Waals heterostructures. *Nature* **567**, 81–86 (2019).
- Jin, C. et al. Identification of spin, valley and moiré quasi-angular momentum of interlayer excitons. *Nat. Phys.* **15**, 1140–1144 (2019).
- Shimazaki, Y. et al. Strongly correlated electrons and hybrid excitons in a moiré heterostructure. *Nature* **580**, 472–477 (2020).

48. Wilson, N. P., Yao, W., Shan, J. & Xu, X. Excitons and emergent quantum phenomena in stacked 2D semiconductors. *Nature* **599**, 383–392 (2021).
49. Gu, J. et al. Dipolar excitonic insulator in a moiré lattice. *Nat. Phys.* **18**, 395–400 (2022).
50. Weston, A. et al. Atomic reconstruction in twisted bilayers of transition metal dichalcogenides. *Nat. Nanotechnol.* **15**, 592–597 (2020).
51. Rosenberger, M. R. et al. Twist angle-dependent atomic reconstruction and Moiré patterns in transition metal dichalcogenide heterostructures. *ACS Nano* **14**, 4550–4558 (2020).
52. Zhao, S. et al. Excitons in mesoscopically reconstructed moiré heterostructures. *Nat. Nanotechnol.* **18**, 572–579 (2023).
53. Xiao, D., Liu, G.-B., Feng, W., Xu, X. & Yao, W. Coupled spin and valley physics in monolayers of MoS₂ and other group-VI dichalcogenides. *Phys. Rev. Lett.* **108**, 196802 (2012).
54. Cao, T. et al. Valley-selective circular dichroism of monolayer molybdenum disulphide. *Nat. Commun.* **3**, 887 (2012).
55. Zeng, H., Dai, J., Yao, W., Xiao, D. & Cui, X. Valley polarization in MoS₂ monolayers by optical pumping. *Nat. Nanotechnol.* **7**, 490–493 (2012).
56. Mak, K. F., He, K., Shan, J. & Heinz, T. F. Control of valley polarization in monolayer MoS₂ by optical helicity. *Nat. Nanotechnol.* **7**, 494–498 (2012).
57. Rivera, P. et al. Valley-polarized exciton dynamics in a 2D semiconductor heterostructure. *Science* **351**, 688–691 (2016).
58. Unuchek, D. et al. Valley-polarized exciton currents in a van der Waals heterostructure. *Nat. Nanotechnol.* **14**, 1104–1109 (2019).
59. Huang, Z. et al. Robust room temperature valley Hall effect of interlayer excitons. *Nano Lett.* **20**, 1345–1351 (2020).
60. Shanks, D. N. et al. Interlayer exciton diode and transistor. *Nano Lett.* **22**, 6599–6605 (2022).
61. Onga, M., Zhang, Y., Ideue, T. & Iwasa, Y. Exciton Hall effect in monolayer MoS₂. *Nat. Mater.* **16**, 1193–1197 (2017).
62. Hao, K., Shreiner, R., Kindseth, A. & High, A. A. Optically controllable magnetism in atomically thin semiconductors. *Sci. Adv.* **8**, eabq7650 (2022).
63. Jin, C. et al. Imaging of pure spin-valley diffusion current in WS₂-WSe₂ heterostructures. *Science* **360**, 893–896 (2018).
64. Ren, L. et al. Optical detection of long electron spin transport lengths in a monolayer semiconductor. *Phys. Rev. Lett.* **129**, 027402 (2022).
65. Fowler-Gerace, L. H., Zhou, Z., Szwed, E. A., Choksy, D. J. & Butov, L. V. Transport and localization of indirect excitons in a van der Waals heterostructure. *Nat. Photonics* **18**, 823–828 (2024).
66. Nikonov, D. E., Imamoglu, A. Bose condensation in two dimensions with disorder: Gross-Pitaevskii approach. Preprint at <https://doi.org/10.48550/arXiv.quant-ph/9806003> (1998).
67. Ivanov, A. L. et al. Origin of the inner ring in photoluminescence patterns of quantum well excitons. *Europhys. Lett.* **73**, 920–926 (2006).
68. Remeika, M. et al. Localization-delocalization transition of indirect excitons in lateral electrostatic lattices. *Phys. Rev. Lett.* **102**, 186803 (2009).
69. Yoshioka, D. & MacDonald, A. H. Double quantum well electron-hole systems in strong magnetic fields. *J. Phys. Soc. Jpn.* **59**, 4211–4214 (1990).
70. Fisher, M. P. A., Weichman, P. B., Grinstein, G. & Fisher, D. S. Boson localization and the superfluid-insulator transition. *Phys. Rev. B* **40**, 546–570 (1989).
71. Laturia, A., Van de Put, M. L. & Vandenbergh, W. G. Dielectric properties of hexagonal boron nitride and transition metal dichalcogenides: from monolayer to bulk. *NPJ 2D Mater. Appl.* **2**, 6 (2018).
72. Wang, J. et al. Optical generation of high carrier densities in 2D semiconductor heterobilayers. *Sci. Adv.* **5**, eaax0145 (2019).
73. Capogrosso-Sansone, B., Söyler, Ş. G., Prokof'ev, N. & Svistunov, B. Monte Carlo study of the two-dimensional Bose-Hubbard model. *Phys. Rev. A* **77**, 015602 (2008).
74. Wang, Z., Chiu, Y.-H., Honz, K., Mak, K. F. & Shan, J. Electrical tuning of interlayer exciton gases in WSe₂ bilayers. *Nano Lett.* **18**, 137–143 (2018).
75. Calman, E. V. et al. Indirect excitons in van der Waals heterostructures at room temperature. *Nat. Commun.* **9**, 1895 (2018).
76. Fowler-Gerace, L. H., Choksy, D. J. & Butov, L. V. Voltage-controlled long-range propagation of indirect excitons in a van der Waals heterostructure. *Phys. Rev. B* **104**, 165302 (2021).
77. Rivera, P. et al. Observation of long-lived interlayer excitons in monolayer MoSe₂-WSe₂ heterostructures. *Nat. Commun.* **6**, 6242 (2015).
78. Calman, E. V. et al. Indirect excitons and trions in MoSe₂/WSe₂ van der Waals heterostructures. *Nano Lett.* **20**, 1869–1875 (2020).
79. Miller, B. et al. Long-lived direct and indirect interlayer excitons in van der Waals heterostructures. *Nano Lett.* **17**, 5229–5237 (2017).
80. Okada, M. et al. Direct and indirect interlayer excitons in a van der Waals heterostructure of hBN/WS₂/MoS₂/hBN. *ACS Nano* **12**, 2498–2505 (2018).
81. Hanbicki, A. T. et al. Double indirect interlayer exciton in a MoSe₂/WSe₂ van der Waals heterostructure. *ACS Nano* **12**, 4719–4726 (2018).
82. Xiong, R. et al. Correlated insulator of excitons in WSe₂/WS₂ moiré superlattices. *Science* **380**, 860–864 (2023).
83. Park, H. et al. Dipole ladders with large Hubbard interaction in a moiré exciton lattice. *Nat. Phys.* **19**, 1286–1292 (2023).
84. Withers, F. et al. Light-emitting diodes by band-structure engineering in van der Waals heterostructures. *Nat. Mater.* **14**, 301–306 (2015).

Acknowledgements

We thank M.M. Fogler and J.R. Leonard for discussions. We especially thank A.H. MacDonald for discussions of IXs in moiré potentials and A.K. Geim for teaching us manufacturing TMD HS. The studies were supported by the DOE Office of Basic Energy Sciences under Award DE-FG02-07ER46449 (L.V.B.). The HS manufacturing was supported by NSF Grant 1905478 (L.V.B.).

Author contributions

L.V.B. designed the project. L.H.F.-G. manufactured the TMD heterostructure. Z.Z., E.A.S., and D.J.C. performed the measurements. Z.Z. and L.V.B. analyzed the data. L.V.B. wrote the manuscript with inputs from all the authors.

Competing interests

The authors declare no competing interests.

Additional information

Supplementary information The online version contains supplementary material available at <https://doi.org/10.1038/s41467-024-53445-5>.

Correspondence and requests for materials should be addressed to L. V. Butov.

Peer review information *Nature Communications* thanks the anonymous reviewer(s) for their contribution to the peer review of this work. A peer review file is available.

Reprints and permissions information is available at <http://www.nature.com/reprints>

Publisher's note Springer Nature remains neutral with regard to jurisdictional claims in published maps and institutional affiliations.

Open Access This article is licensed under a Creative Commons Attribution 4.0 International License, which permits use, sharing, adaptation, distribution and reproduction in any medium or format, as long as you give appropriate credit to the original author(s) and the source, provide a link to the Creative Commons licence, and indicate if changes were made. The images or other third party material in this article are included in the article's Creative Commons licence, unless indicated otherwise in a credit line to the material. If material is not included in the article's Creative Commons licence and your intended use is not permitted by statutory regulation or exceeds the permitted use, you will need to obtain permission directly from the copyright holder. To view a copy of this licence, visit <http://creativecommons.org/licenses/by/4.0/>.

© The Author(s) 2024